



Hot Subdwarf Stars Identified in Gaia DR2 with Spectra of LAMOST DR6 and DR7. II. Kinematics

Yangping Luo¹ , Péter Németh^{2,3} , and Qida Li¹¹ Department of Astronomy, China West Normal University, Nanchong, 637002, People's Republic of China; ypluo@bao.ac.cn² Astronomical Institute of the Czech Academy of Sciences, Fričova 298, CZ-251 65 Ondřejov, Czech Republic³ Astroserver.org, 8533 Malomsok, Hungary

Received 2020 March 3; revised 2020 May 25; accepted 2020 May 30; published 2020 July 23

Abstract

Combining LAMOST radial velocities with Gaia parallaxes and proper motions, we present 3D Galactic space motions and the orbits of 182 single-lined hot subdwarf stars. These stars were identified by Lei et al. in Gaia DR2 with LAMOST DR6 and DR7 spectra. He-rich hot subdwarf stars with $\log(y) \geq 0$ show the largest standard deviations of the Galactic velocity components and orbital parameters, while those with $-1 \leq \log(y) < 0$ exhibit the second largest standard deviations. The two groups of He-deficient stars with $\log(y) < -1$ show similar standard deviations, which are systematically lower compared to He-rich stars. We also present a kinematic population classification of the four hot subdwarf helium groups based on their positions in the $U - V$ velocity diagram, the $J_z -$ eccentricity diagram, and their Galactic orbits. The overall tendency of the fractional distributions of the four hot subdwarf helium groups in the halo, thin disk, and thick disk is largely consistent with the findings reported by Luo et al. based on LAMOST DR5, which appears to support predictions of binary population synthesis. He-deficient stars with $-2.2 \leq \log(y) < -1$ likely originate from a stable Roche lobe overflow channel, He-deficient stars with $\log(y) < -2.2$ from the common envelope ejection channel, and He-rich stars with $\log(y) \geq 0$ from the merger channel of double He white dwarf stars. The fraction of He-rich hot subdwarf stars with $-1 \leq \log(y) < 0$ in the thin disk and the halo is far higher than that in the thick disk, which implies that these stars have different formation channels in the thin disk and in the halo.

Unified Astronomy Thesaurus concepts: [Stellar kinematics \(1608\)](#); [Subdwarf stars \(2054\)](#)

Supporting material: machine-readable table

1. Introduction

Hot subdwarf stars were discovered in 1954 (Greenstein 1954). They are situated at the blueward extension of the horizontal branch (HB) in the Hertzsprung–Russell (HR) diagram, which is also called the extreme horizontal branch (EHB; Heber 2009, 2016). Depending on their spectral appearance, hot subdwarf stars were traditionally classified as O type subdwarf (sdO) and B type subdwarf (sdB) stars (Drilling et al. 2013). They are core helium-burning stars with masses around $0.5M_{\odot}$. Despite showing a similar spectral appearance to O and B main sequence (MS) stars, they turned out to be much smaller than MS stars and much less luminous. As a typical product of stellar evolution, hot subdwarf stars play a vital role in determining the properties of old stellar populations. They are responsible for the phenomenon called UV upturn or UV excess in the spectra of elliptical galaxies and the bulges of spiral galaxies (Han et al. 2007), and dominate the horizontal branch morphology of globular clusters (Han 2008; Lei et al. 2013, 2015). Hot subdwarf stars are also relevant for cosmology, as some of them are candidate progenitors of type Ia supernovae (Justham et al. 2009; Wang et al. 2009; Wang & Han 2010; Geier et al. 2013, 2015a; Wang 2018).

Hot subdwarf stars themselves are peculiar in more than one respect. Several types of pulsating stars have been discovered among hot subdwarfs and these objects turned out to be perfect laboratories for asteroseismic studies (Fontaine et al. 2012; Østensen et al. 2014; Zong et al. 2018; Saio & Jeffery 2019). They display very peculiar element abundance patterns, which mark active diffusion processes in their atmospheres and are also responsible for their low helium abundances (Edelmann

et al. 2003; Heber 2016; Byrne et al. 2018). A few intermediate helium hot subdwarf stars exhibit high abundances of lead, zirconium, strontium, and yttrium, up to 10, 000 times the solar values (Naslim et al. 2011, 2013, 2020; Jeffery et al. 2017; Dorsch et al. 2019; Jeffery & Miszalski 2019). A substantial number of hot subdwarf stars have invisible compact companions, i.e., a neutron star or black hole. Such systems are potential gravitational-wave sources, a speculation that might be resolved by future facilities, such as the Laser Interferometer Space Antenna (LISA; Wu et al. 2018, 2020).

However, the formation of hot subdwarf stars is not well understood. Their formation requires the progenitors to lose almost their entire hydrogen envelope after passing the red giant branch (RGB). The remaining hydrogen envelope does not have enough mass to sustain a hydrogen-burning shell. The reason for the very high mass loss prior to or at the beginning of the helium core flash is still unclear. Different scenarios have been put forward to explain this huge mass loss. The high fraction of binaries among hot subdwarfs suggests that binary evolution involving common envelope (CE) ejection, stable Roche lobe overflow (RLOF), or the merger of double helium white dwarfs (HeWD) are the main formation channels (Webbink 1984; Han et al. 2002, 2003). Population synthesis studies indicated that the first two channels are responsible mainly for sdB stars and the merger channel for He-rich sdO stars (Han et al. 2002; Han 2008; Zhang & Jeffery 2012). In between the sdB and sdO classes both the late hot-flasher scenario (D’Cruz et al. 1996; Moehler et al. 2004; Miller Bertolami et al. 2008) and the merger of helium white dwarfs with low mass main sequence stars (Zhang et al. 2017) have

been suggested to explain the origin of intermediate helium-rich hot subdwarf stars. Although both of these models can explain the observed properties of hot subdwarfs, neither is entirely satisfactory.

With the advent of the Gaia survey (Gaia Collaboration et al. 2018a, 2018b, 2018c, 2018d) and new spectroscopic surveys like LAMOST (the Large Sky Area Multi-Object Fiber Spectroscopic Telescope, also named the ‘‘Guo Shou Jing’’ Telescope; Cui et al. 2012), new and much larger observational samples shed light onto the details of hot subdwarf formation. A total of 166 hot subdwarf stars were identified by Luo et al. (2016) from LAMOST DR1 spectra. Lei et al. (2018) spectroscopically confirmed 294 new hot subdwarf stars in Gaia DR2 with LAMOST DR5 spectra. Geier et al. (2019) published a catalog of 39,800 hot subdwarf candidates selected from Gaia DR2. We have already presented the spectral analyses of 892 non-composite spectra hot subdwarf stars and the kinematics of 747 stars of that catalog by combining LAMOST DR5 and Gaia DR2 data (Luo et al. 2019). Most recently, Lei et al. (2020) published the spectroscopic properties of 182 single-lined spectra hot subdwarf stars selected from Gaia DR2 with spectra from LAMOST DR6 and DR7, without discussing their kinematics.

Because kinematics can put strong constraints on our understanding of hot subdwarf formation, we supplement our previous study (Luo et al. 2019) in this paper. We present the kinematics of the 182 single-lined spectra from Lei et al. (2020) by combining the radial velocities (RVs) extracted from LAMOST spectra with the parallaxes and proper motions from Gaia DR2. In Section 2 we introduce the targets and available data sets and describe the calculations of Galactic space velocities. Orbital parameters are discussed in Section 3. In Section 4, we discuss the Galactic space distribution, space velocity distribution, orbits, population classification, and selection biases for the hot subdwarf groups of different helium abundances. We present our conclusions in Section 5.

2. Targets and Data

2.1. Targets

We analyzed a sample of 182 single-lined hot subdwarf stars observed in Gaia DR2 and LAMOST DR6 and DR7 (Lei et al. 2020). The sample included 89 sdB, 37 sdOB, 26 sdO, 24 He-sdOB, 3 He-sdO, and 3 He-sdB stars. The surface temperature T_{eff} , gravity $\log g$, helium abundance $y = n\text{He}/n\text{H}$ were also collected from Table 1 by Lei et al. (2020) and are shown in Table 1. As described in Luo et al. (2019), these 182 stars can be divided into four groups based on their helium abundances. Generally, the stars were classified as He-rich and He-deficient with respect to the solar helium abundance $\log y = -1$. Furthermore, He-rich and He-deficient stars can also be independently divided into two groups via $\log(y) = 0$ and $\log(y) = -2.2$. The classification scheme could inherently associate these four helium groups with different formation channels in the $T_{\text{eff}} - \log(y)$ diagram (Németh et al. 2012; Luo et al. 2019). As described by Németh et al. (2012), composite spectrum binaries with F and G type companions are relatively easy to identify because they have characteristic features, very different from subdwarfs and a comparable optical brightness. Identifying composite spectra with late G and K type companions is a challenge because of their significantly lower contributions and weaker lines. For these reasons, the

Table 1
Atmospheric Parameters, Space Positions, Orbital Parameters and Galactic Velocities for 182 Single-lined Hot Subdwarf Stars Observed in Gaia DR2 and LAMOST DR6 and DR7

Num	Label	Explanations
1	LAMOST	LAMOST target
2	R.A.deg	Barycentric R.A. (J2000) ^a
3	DEdeg	Barycentric decl. (J2000) ^a
4	T_{eff}	Stellar effective temperature ^b
5	$e_{T_{\text{eff}}}$	Standard error in T_{eff}
6	$\log g$	Stellar surface gravity ^b
7	$e_{\log g}$	Standard error of Stellar surface gravity
8	$\log(y)$	Stellar surface He abundance $y = n\text{He}/n\text{H}$ ^b
9	$e_{\log(y)}$	Standard error in $\log(y)$
10	type	Spectra type ^b
11	$pmRA$	Proper motion in RA
12	e_{pmRA}	Standard error $pmRA$
13	$pmDE$	Proper motion in DE
14	e_{pmDE}	Standard error in $pmDE$
15	D	Gaia DR2 stellar distance
16	e_D	Standard error in stellar distance
17	RV_{el}	Radial velocity from LAMOST spectra
18	$e_{RV_{\text{el}}}$	Standard error in radial velocity
19	X	Galactic position toward Galactic center
20	e_X	Standard error in X
21	Y	Galactic position along Galactic rotation
22	e_Y	Standard error of Y
23	Z	Galactic position toward north Galactic pole
24	e_Z	Standard error of Z
25	U	Galactic radial velocity positive toward Galactic center
26	e_U	Standard error in U
27	V	Galactic rotational velocity along Galactic rotation
28	e_V	Standard error in V
29	W	Galactic velocity toward north Galactic pole
30	e_W	Standard error in W
31	R_{ap}	Apocenter radius ^c
32	$e_{R_{\text{ap}}}$	Standard error in R_{ap}
33	R_{peri}	Pericenter radius ^c
34	$e_{R_{\text{peri}}}$	Standard error in R_{peri}
35	z_{max}	Maximum vertical height ^c
36	$e_{z_{\text{max}}}$	Standard error in z_{max}
37	e	Eccentricity ^c
38	e_e	Standard error in e
39	J_z	Z-component of angular momentum ^c
40	e_{J_z}	Standard error in J_z
41	z_n	Normalized z-extent of the orbit ^c
42	e_{z_n}	Standard error in z_n
43	Pops	Population classification ^d
44	P_{TH}	probability in thin disk
45	P_{TK}	probability in thick disk
46	P_{H}	probability in halo

Notes. The full table can be found in the online version of the paper.

^a At Epoch 2000.0 (ICRS).

^b From Lei et al. (2020).

^c Form the numerical orbit integration.

^d H = Halo; TK = thick disk; TH = thin disk.

(This table is available in its entirety in machine-readable form.)

identification of composite spectra with late type companions also heavily depends on the quality of the spectra. We excluded double-lined composite spectrum systems with noticeable Ca II H&K ($\lambda 3933 \text{ \AA}$ and $\lambda 3968 \text{ \AA}$), Mg I ($\lambda 5183 \text{ \AA}$), or Ca II ($\lambda 8650 \text{ \AA}$) absorption lines. Unfortunately, the near-infrared

region is seriously polluted by sky emission lines in LAMOST spectra and we could not use the Ca II triplet lines.

Binary systems affect the calculations of Galactic velocities and orbits. Although our study focuses on studying only single-lined hot subdwarf stars, we cannot exclude the possibility of having unknown and unresolved binary systems based on a single epoch radial velocity measurement. We consider all stars to be members of the thin-disk, thick-disk, or halo populations until they are further constrained.

2.2. Data

We utilized the spectra of LAMOST DR6 and DR7 to measure the radial velocities of the 182 hot subdwarf stars. The LAMOST spectra are similar to the SDSS data with a resolution of $R \sim 1800$ and wavelength coverage of 3800–9100 Å. The data are described in detail in Luo et al. (2012, 2014). The published radial velocities in the LAMOST catalog are not reliable for hot subdwarf stars because hot subdwarfs are not included in LAMOST stellar templates for RVs. Therefore, we remeasured the radial velocities of these 182 stars and present them in Table 1.

Gaia DR2 provided high-precision positions (α and δ), proper motions ($\mu_\alpha \cos \delta$ and μ_δ), and parallaxes ($\bar{\omega}$) (Gaia Collaboration et al. 2018a, 2018b, 2018c) for all 182 stars. Distances (D) were calculated using $D = 1/\bar{\omega}$. These parameters are shown in Table 1. However, for 20 stars reliable distances cannot be obtained by simply inverting the parallax. Therefore, their distances were replaced with estimated values from the Gaia DR2 distance catalog (Bailer-Jones et al. 2018).

3. Galactic Space Velocities and Orbital Parameters

Based on the distances, radial velocities, and proper motions shown in Table 1, we calculated space velocity components in Cartesian coordinates with the Astropy Python package. We adopted a right-handed Galactocentric Cartesian coordinate system, where the velocity components U , V , and W are positive in the direction toward the Galactic center, Galactic rotation and north Galactic pole, respectively. We set the distance of the Sun from the Galactic center to be 8.4 kpc and the velocity of the local standard of rest (LSR) to be 242 km s^{-1} (Irrgang et al. 2013). For the solar velocity components with respect to the LSR, we assumed $(U_\odot, V_\odot, W_\odot) = (11.1, 12.24, 7.25) \text{ km s}^{-1}$ (Schönrich et al. 2010). Making use of Astropy, we also computed the space position components in a right-handed Galactocentric Cartesian reference frame denoted by (X, Y, Z) .

We applied the Galpy Python package (Bovy 2015) to calculate the Galactic orbital parameters of our program stars. For the calculation of orbits, we adopted the Milky Way potential “MWpotential2014” that comprises a power-law bulge with an exponential cutoff, an exponential disk and a power-law halo component (Bovy 2015). We used the same solar Galactocentric distance and LSR velocity as in Astropy. The Galactic orbital parameters of hot subdwarf stars, such as the apocenter (R_{ap}), pericenter (R_{peri}), eccentricity (e), maximum vertical amplitude (z_{max}), normalized z -extent (z_n), and z -component of the angular momentum (J_z), are extracted from integrating their orbital paths for a time of 5 Gyrs and are listed in Table 1. R_{ap} and R_{peri} represent the maximum and minimum distances of an orbit from the Galactic center, respectively. We

defined the eccentricity by

$$e = \frac{R_{\text{ap}} - R_{\text{peri}}}{R_{\text{ap}} + R_{\text{peri}}}, \quad (1)$$

and the normalized z -extent by

$$z_n = \frac{z_{\text{max}}}{R(z_{\text{max}})}, \quad (2)$$

where R is the Galactocentric distance.

The errors of the space positions and velocity components, as well as of the orbital parameters, were obtained with a Monte Carlo simulation. For each star, 1000 sets of input values with a Gaussian distribution were simultaneously generated and the output parameters were computed together with their errors. Further details on the calculations can be found in Luo et al. (2019) and Luo (2020).

4. Results

4.1. Space Distribution

Figure 1 displays the space positions of the four hot subdwarf helium groups in the $X - Z$ diagrams. The left panel of Figure 1 reveals that the space distributions of the two He-deficient groups do not show any obvious differences. Most stars tend to cluster around the disk and only a few stars are found in the halo. The star density quickly decreases from the disk to the halo and a sharp cutoff appears at $|Z| \sim 1.5$ kpc, which is considered the vertical scale height of the thick disk (Ma et al. 2017).

In contrast, the right panel of Figure 1 shows that the space distributions of the two groups of He-rich stars have a noticeable difference at $|Z| > 1.5$ kpc where the star density of He-rich stars with $\log(y) \geq 0$ is significantly higher than that of stars with $-1 \leq \log(y) < 0$. The difference in space distribution also indicates that the two groups of He-rich stars likely originate from different formation channels.

Comparisons of the left and right panel in the Figure 1 demonstrate that the space density of the two group of He-rich stars has a larger dispersion than the groups of He-deficient stars, which suggests that He-rich and He-deficient hot subdwarf stars have different kinematic origins.

4.2. Galactic Velocity Distribution

Figure 2 exhibits the distribution of the four hot subdwarf helium groups in the $U - V$ velocity diagram. The $U - V$ velocity diagram demonstrates that He-deficient stars can be found mostly around the LSR, while He-rich stars are more widely scattered in the whole region. In order to identify the Galactic population memberships of the stars, we also plot the two dotted ellipses as shown in Figure 1 of Martin et al. (2017). They mark the 3σ limits of thin-disk and thick-disk WDs (Pauli et al. 2006), respectively.

In order to illustrate the kinematics of the total velocity for the four hot subdwarf helium groups, Figure 3 displays the kinetic energy $2E_{\text{kin}}/m = U^2 + V^2 + W^2$ versus rotational velocity (V) diagram. The higher the value of the kinetic energy $2E_{\text{kin}}/m$, the more elliptic the orbit of the star. We also plotted the isovelocity curves perpendicular to the Galactic rotation, where $V_\perp = (U^2 + V^2)^{1/2}$. The higher the value of the V_\perp , the hotter is the kinematic temperature. As described by Luo et al. (2019), most of stars are clustered around the LSR in a “banana” shaped region alongside the $V_\perp = 0 \text{ km s}^{-1}$

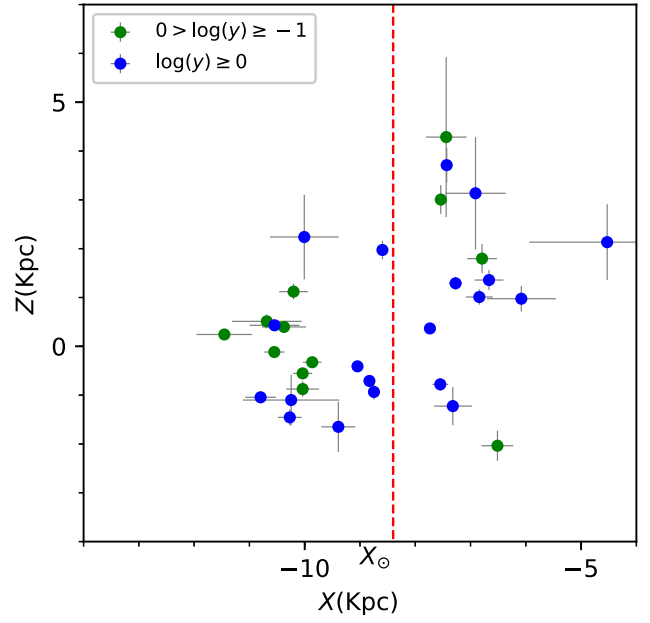
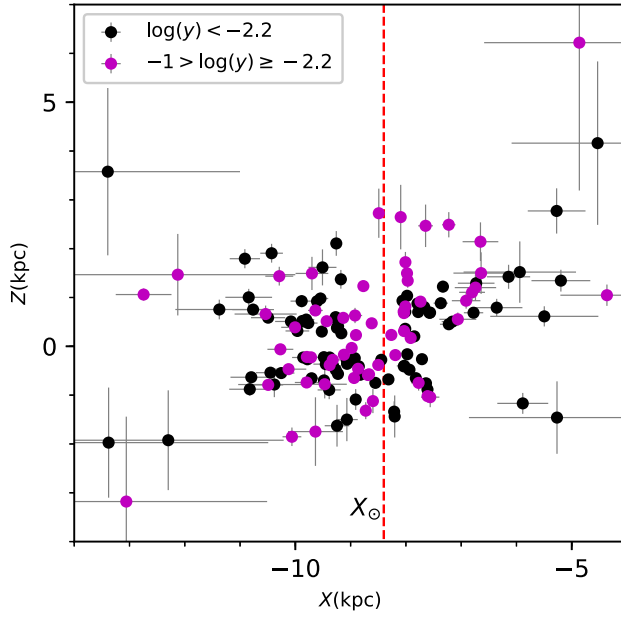


Figure 1. Space positions of hot subdwarf stars in Cartesian Galactic $X - Z$ coordinates. He-deficient stars are shown in the left panel and He-rich stars are displayed in the right panel. The dashed line marks the solar position.

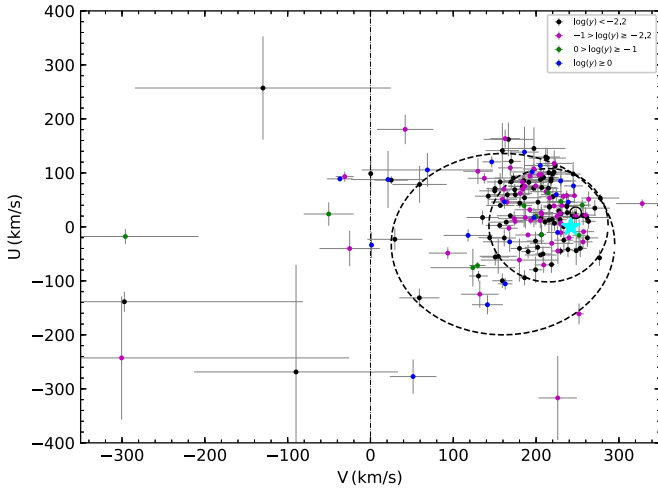


Figure 2. $U - V$ velocity diagram for the four hot subdwarf helium groups. Two dashed ellipses denote the 3σ limits for the thin-disk and thick-disk populations, respectively (Pauli et al. 2006). The cyan star symbol represents the local standard of rest (LSR).

isoveLOCITY curve, which means that they are kinematically cool and likely have more circular orbits. A few stars are located farther away from the $V_{\perp} = 0 \text{ km s}^{-1}$ isoveLOCITY curve, where He-rich stars with $\log(y) \geq 0$ have a higher fraction. These are kinematically hot stars with likely more eccentric orbits. The sample also exhibits a sharp cut near 110 km s^{-1} . The few stars to the left of this velocity limit show a larger scatter and belong to the halo population (Altmann et al. 2004). In this region, the proportion of He-rich stars with $\log(y) \geq 0$ is more than 25%.

Table 2 lists the mean values and standard deviations of the Galactic velocity components for the four hot subdwarf helium groups. We find that He-rich stars with $\log(y) \geq 0$ show the largest standard deviations of the Galactic velocity components in all four hot subdwarf helium groups and He-rich stars with $-1 \leq \log(y) < 0$ display the second largest standard deviation. The two groups of He-deficient stars exhibit similar values of standard deviations.

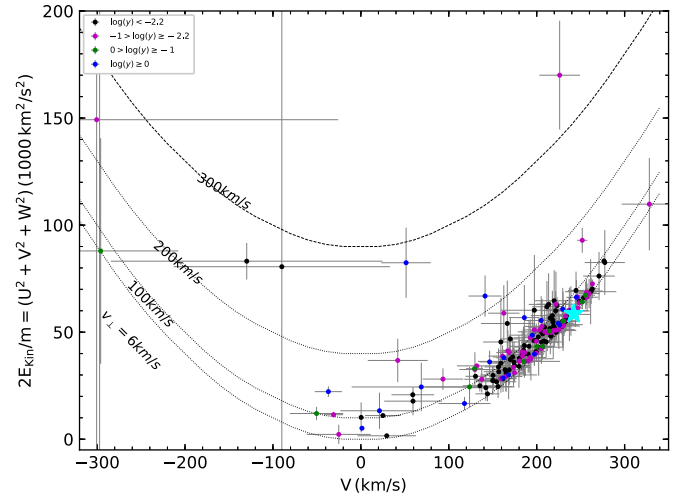


Figure 3. Galactic rotational velocity V against the total kinetic energy $2E_{\text{kin}}/m = U^2 + V^2 + W^2$ for the four hot subdwarf helium groups. The parabolic curves denote the isoveLOCITY perpendicular to the direction of Galactic rotation, where $V_{\perp} = (U^2 + V^2)^{1/2}$. The cyan star symbol represents the local standard of rest (LSR).

These results are in good agreement with the findings of Luo et al. (2019). The diverse range of kinematic velocities support the argument that He-rich hot subdwarf stars with $\log(y) \geq 0$ likely originate from different formation channels.

4.3. Galactic Orbits

Two important orbital parameters are the z -component of the angular momentum J_z and the eccentricity e of the orbit. They are used to distinguish different populations. Figure 4 shows the distribution of the four hot subdwarf helium groups in the $J_z - e$ diagram. We also show the two regions defined by Pauli et al. (2003): Region A confines thin-disk stars clustering to an area of low eccentricity, and J_z around $1800 \text{ kpc km s}^{-1}$; Region B encompasses thick-disk stars with higher eccentricities and lower angular momenta. Outside these two regions,

Table 2
Mean Values and Standard Deviations of the Galactic Velocities and the Galactic Orbital Parameters: Eccentricity (e), Normalized z -extent (z_n), Maximum Vertical Amplitude (z_{\max}), Apocenter (R_{ap}) and Pericenter (R_{peri}) for the Four Hot Subdwarf Helium Groups

Subsample	N	\bar{U}	σ_U	\bar{V}	σ_V	\bar{W}	σ_W	$\overline{U^2 + V^2 + W^2}$	$\sigma_{U^2+V^2+W^2}$	\bar{e}	σ_e	\bar{z}_n	σ_{z_n}	\bar{z}_{\max}	$\sigma_{z_{\max}}$	$\overline{R_{\text{ap}}}$	$\sigma_{R_{\text{ap}}}$	$\overline{R_{\text{peri}}}$	$\sigma_{R_{\text{peri}}}$
All stars	182	30	62	203	35	0	36	46 458	16 817	0.23	0.13	0.12	0.08	1.14	0.70	9.94	1.84	5.98	2.45
$\log(y) \geq 0$	20	39	76	148	82	4	60	42 938	20 150	0.41	0.32	0.29	0.22	2.42	1.75	10.17	2.46	4.79	3.22
$-1 \leq \log(y) < 0$	12	3	43	204	44	-2	49	47 907	19 653	0.27	0.20	0.22	0.23	2.38	2.37	10.96	1.51	6.86	2.99
$-2.2 \leq \log(y) < -1$	57	35	57	205	33	-1	31	46 568	12 457	0.20	0.10	0.12	0.08	0.99	0.53	9.64	1.46	6.13	2.15
$\log(y) < -2.2$	89	29	63	203	35	3	35	46 962	16 640	0.24	0.14	0.12	0.07	1.17	0.73	9.94	1.89	6.02	2.25

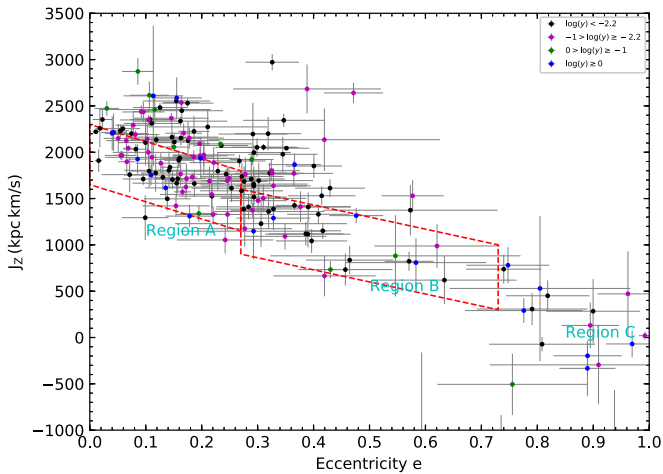


Figure 4. Z -component of the angular momentum vs. eccentricity (e) for the four hot subdwarf helium groups. The two parallelograms denote Region A (thin disk) and Region B (thick disk) (Pauli et al. 2006).

defined as region C, halo star candidates are found. The majority of stars show a continuous distribution from Region A to Region B without an obvious dichotomy. Only a few stars lie in Region C and they are separated by a noticeable gap from Region B and Region C. In Region C, He-rich stars with $\log(y) \geq 0$ have a very high fraction.

In Table 2 we give the mean values and standard deviations of the orbital parameters: eccentricity, normalized z -extent, maximum vertical amplitude, apocenter, and pericenter. The standard deviation of the orbital parameters is similar to that of the Galactic velocity components. He-rich stars with $\log(y) \geq 0$ show the largest standard deviation of the orbital parameters and He-rich stars with $-1 \leq \log(y) < 0$ display the second largest standard deviation. The two groups of He-deficient stars show similar values of standard deviations. These results are in good agreement with earlier findings (Martin et al. 2017; Luo et al. 2019).

4.4. Galactic Population Classifications

We primarily adopted the $U - V$ diagram, $J_z - e$ diagram, and the maximum vertical amplitude z_{\max} to distinguish the Galactic populations of hot subdwarfs. To ensure correct population assignments, all orbits were visually inspected to supplement the automatic classifications. The detailed classification scheme was described by Martin et al. (2017) and Luo et al. (2019). Thin-disk stars are situated within the 3σ thin-disk contour in the $U - V$ diagram and Region A in the $J_z - e$ diagram. Their orbits show a small extension in the Galactocentric distance R and the Galactic plane Z directions and have $z_{\max} < 1.5$ kpc. Thick disk stars lie within the 3σ thick-disk contour and in Region B. The extensions of their orbits in the R and the Z directions are larger than that of thin-disk stars, but do not reach the region of halo stars. Halo stars lie outside Region A and B, as well as outside the 3σ thick-disk contour. Their orbits show high extensions in R and Z . There are also some halo stars with an extension in R larger than 18kpc, or the vertical distance from the Galactic plane Z larger than 6kpc. Table 3 gives the number of stars in the four hot subdwarf helium groups classified as halo, thin, or thick-disk stars and Figure 5 displays their fractions in the halo, thin disk, and thick disk.

Table 3
Population Classification and Relative Contributions of the Four Hot Subdwarf Helium Groups

Subsample	N	Thin Disk	Thick Disk	Halo
All stars	182	83	73	26
$\log(y) \geq 0$	19	5	8	6
$-1 \leq \log(y) < 0$	13	7	2	4
$-2.2 \leq \log(y) < -1$	60	32	20	8
$\log(y) < -2.2$	90	39	43	8

The general trends in the distributions of the four hot subdwarf helium groups observed in LAMOST DR6 and DR7 can be matched with the results reported in LAMOST DR5 (Luo et al. 2019). A study on the structure of the Milky Way (Xiang et al. 2017) demonstrated that the different Galactic populations (thin-disk, thick-disk, and halo) reflect different age stellar populations. The binary population synthesis calculations of Han (2008) gave the fractions of hot subdwarf stars from three different formation channels (stable RLOF, CE ejection, and the merger of double HeWDs) at various stellar population ages. Although the exact values of the fractions are not consistent with the predictions of binary population synthesis (Han et al. 2003; Han 2008), we could make a comparison of the overall tendency of the fractional distributions.

The frequency of He-rich hot subdwarf stars with $\log(y) \geq 0$ monotonically increases from 6% in the thin disk to 23% in the halo. This trend is in a good agreement with the predictions of the merger channel of double HeWDs. Although many observations could outline two groups of He-deficient stars in the $T_{\text{eff}} - \log g$ and $T_{\text{eff}} - \log(y)$ diagrams separated by a gap in He abundance at $\log(y) = -2.2$ (Edelmann et al. 2003; Lisker et al. 2005; Stroeger et al. 2007; Hirsch 2009; Geier et al. 2011, 2015b; Németh et al. 2012; Luo et al. 2016, 2019; Lei et al. 2018, 2020), their formation channels are not understood well. Németh et al. (2012) found that hot subdwarf binary systems with F and G type companions, which are predominantly long-period binary candidates from the stable RLOF channel, appear in the two groups of He-deficient stars but show higher fractions among sdB stars with $-2.2 \leq \log(y) < -1$. However, reviews of larger samples (Kawka et al. 2015; Kupfer et al. 2015) found that both short-period and long-period hot subdwarf binary systems occur in each sdB group. We found that the fraction of He-deficient stars with $\log(y) < -2.2$ is in good agreement with the predictions of the CE ejection channel and the fraction of He-deficient sdB stars with $-2.2 \leq \log(y) < -1$ agrees with the predictions of the stable RLOF channel if the excluded composite binary systems were all considered to have sdB stars with $-2.2 \leq \log(y) < -1$ in LAMOST DR5. The vast majority of the identified composite spectra show signatures of F or early G type companions. To determine the nature of hot subdwarfs in these systems we will need spectral decomposition. The distribution of single-lined He-deficient hot subdwarf stars observed in LAMOST DR6 and DR7 (Lei et al. 2020) is in good agreement with the distribution of single-lined He-deficient stars derived from LAMOST DR5 data (Luo et al. 2019). These samples support the predicted fractional contributions of the formation channels (Han et al. 2003; Han 2008).

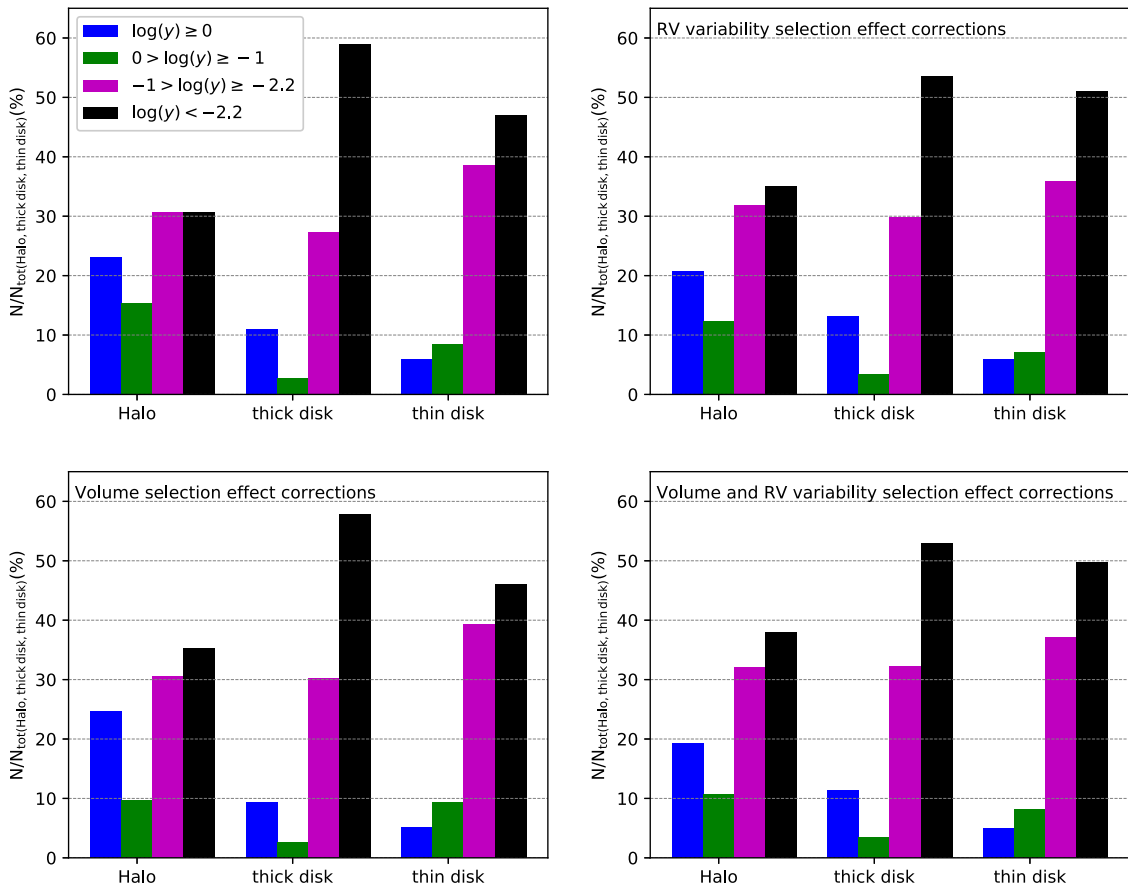


Figure 5. Fractional distributions of the four hot subdwarf helium groups for the halo, thick-disk, and thin-disk populations. Upper left: uncorrected. Upper right: RV variability selection-effect corrections. Lower left: volume selection-effect corrections. Lower right: volume and RV variability selection-effect corrections.

Finally, the formation of He-rich hot subdwarf stars with $-1 \leq \log(y) < 0$ remains a puzzle. The fraction of He-rich hot subdwarf stars with $-1 \leq \log(y) < 0$ increases to 15% in the halo after decreasing from $\sim 8\%$ in the thin disk to $\sim 3\%$ in the thick disk, which is consistent with that of LAMOST DR5. Their frequency implies that He-rich hot subdwarf stars with $-1 \leq \log(y) < 0$ in the thin disk and the halo may have different formation channels. Recent observations (Jeffery et al. 2017; Dorsch et al. 2019; Jeffery & Miszalski 2019; Naslim et al. 2020) found that He-rich hot subdwarf stars with $-1 \leq \log(y) < 0$ show a strong enrichment of heavy elements. The reason for this enrichment is still unclear. Future kinematic studies may help shed light on the poorly understood physical processes behind the strong enrichment of heavy elements.

4.5. Discussion of Selection Biases

Radial velocity surveys (e.g., Maxted et al. 2001; Morales-Rueda et al. 2003; Copperwheat et al. 2011; Geier et al. 2011) of sdB stars showed that about 50% of sdB stars reside in close binary systems with either a cool MS star or a WD companion. Napiwotzki et al. (2004) reported a binary fraction of 39% of sdB stars from the ESO Supernova type Ia Progenitor survey (SPY). Recently, Kawka et al. (2015) reported a binary fraction of 37% of hot subdwarf stars selected from the GALEX all-sky survey and showed RV amplitudes ranging from a few tens to hundreds of km s^{-1} . The kinematic analysis based on just one epoch in RV is therefore intrinsically uncertain. With the binary population statistics of Kawka et al. (2015), we performed

Monte Carlo simulations for our sample. We applied the binary fraction of 37% for single-lined subdwarf stars and the distribution of RV amplitudes to correct for systematics due to the unknown RV. For each binary system, we assumed a circular orbit in the form $RV(t) = \gamma + K \sin \phi$, where K is the RV amplitude, γ is the system velocity, and ϕ is the orbital phase. The orbital phase ϕ was chosen from a uniform distribution from 0 to 2π . 3000 system RVs were produced for each individual star. Combining the distances, proper motions, and their errors, we calculated their Galactic space velocity components and orbits. We obtained the probabilities of the Galactic populations on each individual star and listed in Table 1. The upper right panel of Figure 5 shows the RV variability selection-effect-corrected fractional distributions of the four hot subdwarf helium groups for the halo, thick-disk, and thin-disk populations. The impact of the RV variability selection effect on the fractional distributions is less than 5% of the number of stars in a group.

Using the effective temperature (T_{eff}) and surface gravity (g) we determined the total luminosity (in L_{\odot}) by assuming for all stars a sample-average mass of $0.47M_{\odot}$ (Fontaine et al. 2012). The upper left panel of Figure 6 displays the luminosity versus distance of the sample. There is no clear correlation between luminosity and distance for the sample.

Thanks to Gaia DR2, Geier et al. (2019) compiled an all-sky catalog of 39,800 hot subdwarf star candidates using the means of color, absolute magnitude, and reduced proper motion cuts. Except for the Galactic plane, the catalog is nearly complete up to about 1.5 kpc. The upper right panel of

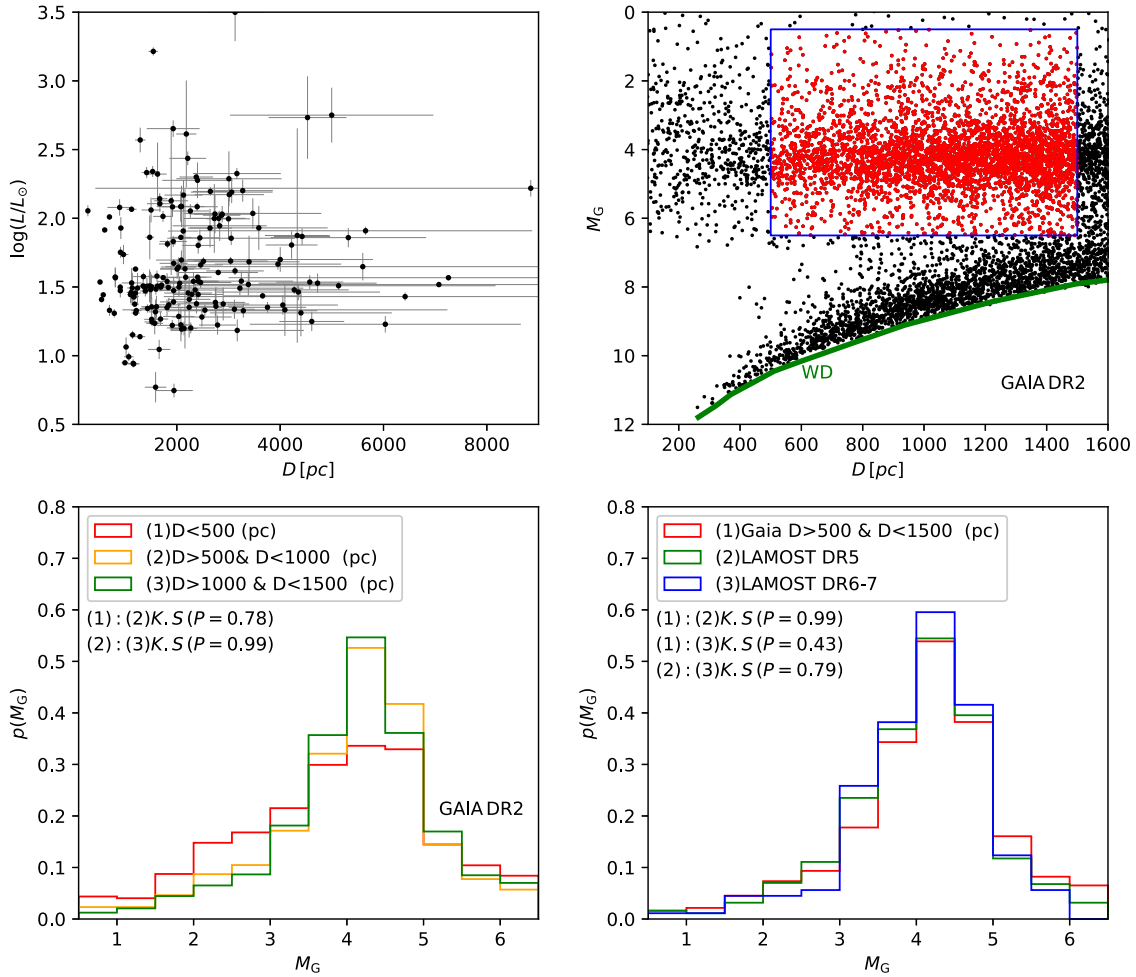


Figure 6. Selection-effect corrections. Upper left: luminosity (assuming a stellar mass of $0.47M_{\odot}$) vs. Gaia distance for 182 hot subdwarf stars in LAMOST DR6 and DR7. Upper right: Gaia absolute G magnitude vs. Gaia distance for hot subdwarf stars in Gaia DR2 (Geier et al. 2019). The green line denotes the cutoff value for WDs. Lower left: distribution functions of Gaia absolute G magnitude for three distance intervals for hot subdwarf stars in Gaia DR2. Lower right: comparison of the distribution functions of hot subdwarf stars in LAMOST DR5, DR6, DR7, and Gaia DR2.

Figure 6 illustrates the absolute Gaia G magnitude $M_G = G + 5 \log(D) - 10 - A_G$ versus distance D (in pc). In order to avoid contamination due to WDs at the faint limit, we restricted the sample to objects with $-0.65 \leq M_G < -0.5$. The lower left panel of Figure 6 displays the distribution function of M_G for objects that lie in three distance intervals, respectively. The last two intervals show quite similar distribution functions and the Kolmogorov–Smirnov (K–S) test gives a P value of 0.99. Therefore, the objects with $500 < D < 1500$ in Gaia DR2 are expected to be volume complete. The lower right panel of Figure 6 shows comparisons of the distribution function of M_G for hot subdwarf stars with $500 < D < 1500$ in Gaia DR2, objects in LAMOST DR5 (Luo et al. 2019), DR6 and DR7 (Lei et al. 2020). We consider the sample of hot subdwarfs in LAMOST DR5 to be complete. In the lower left panel of Figure 5 we give the volume selection-effect-corrected fractional distributions of the four hot subdwarf helium groups for the halo, thick-disk, and thin-disk populations. The influence of the volume selection effect on the results is estimated to be less than 5% of the number of stars within a group. We also present the volume and RV variability selection effect corrected fractional distributions of the four hot subdwarf helium groups for the halo, thick-disk, and thin-disk populations in the lower left panel of Figure 5. A total impact

of these two effects is less than 8% of the number of stars within each group. We can see that the overall tendency of the fractional distributions of the four hot subdwarf helium groups in the halo, thin disk, and thick disk from DR6 and DR7 are consistent with the findings reported by Luo et al. (2019) based on LAMOST DR5.

5. Conclusions

To supplement our previous work (Luo et al. 2019), we explored the kinematics of 182 single-lined hot subdwarf stars selected by Lei et al. (2020) in Gaia DR2 with spectra from LAMOST DR6 and DR7. Making use of the parallaxes and proper motions of Gaia DR2 and the radial velocities measured from LAMOST spectra, we computed the Galactic space positions, Galactic velocity components, and Galactic orbits. Following our previous work (Luo et al. 2019), these stars were classified into four groups based on their helium abundances. From the kinematic properties of the four hot subdwarf helium groups the following conclusions can be drawn:

1. The space distributions show that the space density of He-rich stars have a larger dispersion than the groups of He-deficient stars from the thin disk to the halo. The latter two groups do not show any obvious differences in space

distribution, but the former two groups exhibit a noticeable difference around $|Z| = 1.5$ kpc where the star density of He-rich stars with $\log(y) > 0$ is far higher than that of stars with $-1 \leq \log(y) < 0$. As described in Luo et al. (2019), the space distribution differences indicate that He-rich and He-deficient stars likely originate from different formation channels.

- Likewise, the $U - V$ velocity diagram and the kinetic energy $2E_{\text{kin}}/m = U^2 + V^2 + W^2$ versus rotational velocity (V) diagram demonstrate that He-deficient stars tend to group around the LSR, while He-rich stars are widely scattered in the whole parameter space. He-rich stars with $\log(y) > 0$ have a higher proportion than stars with $-1 \leq \log(y) < 0$. In addition, He-rich stars with $\log(y) > 0$ display the largest standard deviation of the Galactic velocity components and orbital parameters, while He-rich stars with $-1 \leq \log(y) < 0$ represent the second largest standard deviation. The two groups of He-deficient stars with $\log(y) < -2.2$ display a similar value of standard deviation. These results also support that these four hot subdwarf helium groups are likely to originate from different formation channels (Luo et al. 2019).
- We have also presented a kinematic population classification of the four hot subdwarf helium groups based on their positions in the $U - V$ velocity diagram, $J_z - e$ diagram and their Galactic orbits. The relative contributions of the four hot subdwarf helium groups to the halo, thin disk, and thick disk can be largely matched with the results derived from LAMOST DR5 (Luo et al. 2019), which appears to support the predictions of binary population synthesis (Han et al. 2003; Han 2008). He-deficient stars with $-2.2 \leq \log(y) < -1$ likely originate from the stable RLOF channel, He-deficient stars with $\log(y) < -2.2$ from the CE ejection channel, and He-rich stars with $\log(y) \geq 0$ from the merger channel of double HeWDs. As shown by Luo et al. (2019), the fraction of He-rich hot subdwarf stars with $-1 \leq \log(y) < 0$ in the thin disk and halo is higher than that in the thick disk, which suggests that these stars may have different formation channels in the thin disk and the halo.

We thank the anonymous reviewer for their comments, which significantly improved the paper. The research presented here is supported by the National Natural Science Foundation of China under grant no. U1731111 and the Fundamental Research Fund of China West Normal University under grant no. 17YC511. P.N. acknowledges support from the Grant Agency of the Czech Republic (GAČR 18-20083S). Guoshoujing Telescope (the Large Sky Area Multi-Object Fiber Spectroscopic Telescope LAMOST) is a National Major Scientific Project built by the Chinese Academy of Sciences. Funding for the project has been provided by the National Development and Reform Commission. LAMOST is operated and managed by the National Astronomical Observatories, Chinese Academy of Sciences. This work has made use of data from the European Space Agency (ESA) mission Gaia (<https://www.cosmos.esa.int/gaia>), processed by the Gaia Data Processing and Analysis Consortium (DPAC, <https://www.cosmos.esa.int/web/gaia/dpac/consortium>). Funding for the DPAC has been provided by national institutions, in

particular the institutions participating in the Gaia Multilateral Agreement. This research has used the services of www.Astroservers.org.

Software: astropy (Astropy Collaboration et al. 2013, 2018), TOPCAT (v4.6; Taylor 2005, 2019), galpy (Bovy 2015).

ORCID iDs

Yangping Luo  <https://orcid.org/0000-0003-3736-6076>
Péter Németh  <https://orcid.org/0000-0003-0963-0239>

References

- Altmann, M., Edelmann, H., & de Boer, K. S. 2004, *A&A*, 414, 181
Astropy Collaboration, Price-Whelan, A. M., Sipőcz, B. M., et al. 2018, *AJ*, 156, 123
Astropy Collaboration, Robitaille, T. P., Tollerud, E. J., et al. 2013, *A&A*, 558, A33
Bailer-Jones, C. A. L., Rybizki, J., Fouesneau, M., et al. 2018, *AJ*, 156, 58
Bovy, J. 2015, *ApJS*, 216, 29
Byrne, C. M., Jeffery, C. S., Tout, C. A., & Hu, H. 2018, *MNRAS*, 475, 4728
Copperwheat, C. M., Morales-Rueda, L., Marsh, T. R., et al. 2011, *MNRAS*, 415, 1381
Cui, X.-Q., Zhao, Y.-H., Chu, Y.-Q., et al. 2012, *RAA*, 12, 1197
D'Cruz, N. L., Dorman, B., Rood, R. T., & O'Connell, R. W. 1996, *ApJ*, 466, 359
Dorsch, M., Latour, M., & Heber, U. 2019, *A&A*, 630, A130
Drilling, J. S., Jeffery, C. S., Heber, U., Moehler, S., & Napiwotzki, R. 2013, *A&A*, 551, A31
Edelmann, H., Heber, U., Hagen, H.-J., et al. 2003, *A&A*, 400, 939
Fontaine, G., Brassard, P., Charpinet, S., et al. 2012, *A&A*, 539, A12
Gaia Collaboration, Brown, A. G. A., Vallenari, A., et al. 2018a, *A&A*, 616, A1
Gaia Collaboration, Babusiaux, C., van Leeuwen, F., et al. 2018b, *A&A*, 616, A10
Gaia Collaboration, Katz, D., Antoja, T., et al. 2018c, *A&A*, 616, A11
Gaia Collaboration, Helmi, A., van Leeuwen, F., et al. 2018d, *A&A*, 616, A12
Geier, S., Fürst, F., Ziegerer, E., et al. 2015a, *Sci*, 347, 1126
Geier, S., Hirsch, H., Tillich, A., et al. 2011, *A&A*, 530, A28
Geier, S., Kupfer, T., Heber, U., et al. 2015b, *A&A*, 577, A26
Geier, S., Marsh, T. R., Wang, B., et al. 2013, *A&A*, 554, A54
Geier, S., Maxted, P. F. L., Napiwotzki, R., et al. 2011, *A&A*, 526, A39
Geier, S., Raddi, R., Gentile Fusillo, N. P., & Marsh, T. R. 2019, *A&A*, 621, A38
Greenstein, J. L. 1954, *AJ*, 59, 322
Han, Z. 2008, *A&A*, 484, L31
Han, Z., Podsiadlowski, P., & Lynas-Gray, A. E. 2007, *MNRAS*, 380, 1098
Han, Z., Podsiadlowski, P., Maxted, P. F. L., & Marsh, T. R. 2003, *MNRAS*, 341, 669
Han, Z., Podsiadlowski, P., Maxted, P. F. L., Marsh, T. R., & Ivanova, N. 2002, *MNRAS*, 336, 449
Heber, U. 2009, *ARA&A*, 47, 211
Heber, U. 2016, *PASP*, 128, 082001
Hirsch, H. A. 2009, PhD thesis, Friedrich-Alexander Univ. Erlangen-Nürnberg
Irrgang, A., Wilcox, B., Tucker, E., & Schiefelbein, L. 2013, *A&A*, 549, A137
Jeffery, C. S., Baran, A. S., Behara, N. T., et al. 2017, *MNRAS*, 465, 3101
Jeffery, C. S., & Miszalski, B. 2019, *MNRAS*, 489, 1481
Justham, S., Wolf, C., Podsiadlowski, P., & Han, Z. 2009, *A&A*, 493, 1081
Kawka, A., Vennes, S., O'Toole, S., et al. 2015, *MNRAS*, 450, 3514
Kupfer, T., Geier, S., Heber, U., et al. 2015, *A&A*, 576, A44
Lei, Z., Chen, X., Zhang, F., & Han, Z. 2015, *MNRAS*, 449, 2741
Lei, Z., Zhao, J., Németh, P., et al. 2020, *ApJ*, 889, 117
Lei, Z., Zhao, J., Németh, P., & Zhao, G. 2018, *ApJ*, 868, 70
Lei, Z.-X., Chen, X.-F., Zhang, F.-H., & Han, Z. 2013, *A&A*, 549, A145
Lisker, T., Heber, U., Napiwotzki, R., et al. 2005, *A&A*, 430, 223
Luo, A., Zhang, J., Chen, J., et al. 2014, IAU Symp. 298, Setting the Scene for Gaia and LAMOST (Cambridge: Cambridge Univ. Press), 428
Luo, A.-L., Zhang, H.-T., Zhao, Y.-H., et al. 2012, *RAA*, 12, 1243
Luo, Y. 2020, *NewA*, 78, 101363
Luo, Y., Németh, P., Deng, L., et al. 2019, *ApJ*, 881, 7
Luo, Y.-P., Németh, P., Liu, C., Deng, L.-C., & Han, Z.-W. 2016, *ApJ*, 818, 202
Ma, X., Hopkins, P. F., Wetzell, A. R., et al. 2017, *MNRAS*, 467, 2430
Martin, P., Jeffery, C. S., Naslim, N., & Woolf, V. M. 2017, *MNRAS*, 467, 68

- Maxted, P. F. L., Heber, U., Marsh, T. R., et al. 2001, *MNRAS*, **326**, 1391
- Miller Bertolami, M. M., Althaus, L. G., Unglaub, K., & Weiss, A. 2008, *A&A*, **491**, 253
- Moehler, S., Sweigart, A. V., Landsman, W. B., Hammer, N. J., & Dreizler, S. 2004, *A&A*, **415**, 313
- Morales-Rueda, L., Maxted, P. F. L., Marsh, T. R., et al. 2003, *MNRAS*, **338**, 752
- Napiwotzki, R., Karl, C. A., Lisker, T., et al. 2004, *Ap&SS*, **291**, 321
- Naslim, N., Jeffery, C. S., Behara, N. T., & Hibbert, A. 2011, *MNRAS*, **412**, 363
- Naslim, N., Jeffery, C. S., Hibbert, A., & Behara, N. T. 2013, *MNRAS*, **434**, 1920
- Naslim, N., Jeffery, C. S., & Woolf, V. M. 2020, *MNRAS*, **491**, 874
- Németh, P., Kawka, A., & Vennes, S. 2012, *MNRAS*, **427**, 2180
- Østensen, R. H., Telting, J. H., Reed, M. D., et al. 2014, *A&A*, **569**, A15
- Pauli, E.-M., Napiwotzki, R., Altmann, M., et al. 2003, *A&A*, **400**, 877
- Pauli, E.-M., Napiwotzki, R., Heber, U., Altmann, M., & Odenkirchen, M. 2006, *A&A*, **447**, 173
- Saio, H., & Jeffery, C. S. 2019, *MNRAS*, **482**, 758
- Schönrich, R., Binney, J., & Dehnen, W. 2010, *MNRAS*, **403**, 1829
- Stroeer, A., Heber, U., Lisker, T., et al. 2007, *A&A*, **462**, 269
- Taylor, M. 2019, in ASP Conf. Ser. 523, *Astronomical Data Analysis Software and Systems XXVIII*, ed. P. J. Teuben, M. W. Pound, B. A. Thomas, & E. M. M. Warner (San Francisco, CA: ASP), 43
- Taylor, M. B. 2005, *adass XIV*, 347, 29
- Wang, B. 2018, *RAA*, **18**, 049
- Wang, B., & Han, Z. 2010, *A&A*, **515**, A88
- Wang, B., Meng, X., Chen, X., & Han, Z. 2009, *MNRAS*, **395**, 847
- Webbink, R. F. 1984, *ApJ*, **277**, 355
- Wu, Y., Chen, X., Chen, H., et al. 2020, *A&A*, **634**, A126
- Wu, Y., Chen, X., Li, Z., et al. 2018, *A&A*, **618**, A14
- Xiang, M., Liu, X., Shi, J., et al. 2017, *ApJS*, **232**, 2
- Zhang, X., Hall, P. D., Jeffery, C. S., & Bi, S. 2017, *ApJ*, **835**, 242
- Zhang, X., & Jeffery, C. S. 2012, *MNRAS*, **419**, 452
- Zong, W., Charpinet, S., Fu, J.-N., et al. 2018, *ApJ*, **853**, 98